Journal of
Renewable Energy Research and Applications (RERA)

*Vol. 5, No 2, 2024, 195-209* *DOI: 10.22044/rera.2023.12943.1213*

# A Comparative Investigation of L-Serpentine and Single Serpentine Flow Fields Efficiency in Proton Exchange Membrane Fuel Cells using Computational Fluid Dynamics

G. Amarnath[1*], A. V. Babu[1], K. G. Babu[2] and K. Bhosale[1]

*1. Mechanical Engineering Department, National Institute of Technology, Warangal, Telengana, India.*
*2. Mechanical Engineering Department, National Institute of Technology Andhra Pradesh, Tadepalligudem, India.*

Received Date 12 April 2023; Revised Data 16 Msy 2023; Accepted Date 20 May 2023
**Corresponding author:amargundala@gmail.com (G. Amarnath)*

**Abstract**
Fuel cells have been identified as a promising technology to meet future electric power requirements. Out of various fuel cells, Proton Exchange Membrane Fuel Cells (PEMFCs) have been staged up as they can operate at low temperatures and also have a high power density. In this article, the flow field design of a Single Serpentine Flow Field (SSFF) has been modified to L-Serpentine Flow Field (LSFF) in order to reduce thermal and water management problems in PEMFC. A numerical study is conducted on 441 $mm^2$ active area at 70 $^0$C and 3 atm operating conditions to evaluate various flow characteristics by comparing LSFF with SSFF, and it is observed that temperature and species flux distribution in LSFF enhanced significantly. The modification of the flow field yields remarkable improvements in various aspects. These enhancements include a more uniform distribution of membrane water content, an impressive 8% increase in $O_2$ consumption, and a remarkable 22% improvement in product evacuation demonstration by the $H_2O$ species profile, attributed to a 40% reduction in product travel distance. Additionally, a noteworthy 10% increase in power density is achieved. Despite a slight increase in pressure drop due to the additional bends and turns in the modified flow field, the impact on power density remains insignificant. These findings highlight the immense potential of the modified flow field to significantly enhance performance.

**Keywords:** *PEM fuel cells, flow field design, water management, thermal management, serpentine flow fields.*

**Highlights**

1. The L-serpentine flow field was designed to address thermal and water management issues in PEMFCs.
2. Numerical simulations were conducted on a 441 $mm^2$ active area at 70$^0$C and 3 atm to compare the SSFF and LSFF designs.
3. The LSFF showed enhanced temperature, membrane water content distribution, $O_2$ consumption, and $H_2O$ species profile, leading to a 10% increase in power density.
4. The LSFF's 40% reduced product travel length contributed to better product evacuation, while a slight increase in pressure drop did not affect power density.

## 1. Introduction

World's power demand for transportation and for home appliances is increasing expeditiously. Despite imposed restrictions on carbon foot print methods for power production. Therefore, a growing nation like India is looking for pollution-free energy production methods. In order to meet this requirement, the government is planning to reduce India's dependency on thermal power plants to 50-55% by 2030 (that is 60% till year 2022) and switch over to renewable energy. since India accounts for 49% of total CO2 emissions, compared to the global average of 41% [1]. Now under the gambit of alternative energy, world is looking for promising technologies including battery power and fuel cells that ensure pollution-free energy[2]. Furthermore, batteries are known to have a specific energy ranging from 100 to 250 Wh/kg, while Proton Exchange Membrane Fuel

Cells (PEMFCs) exhibit a higher specific energy range from 600 to 1000 Wh/kg[3].

Renewable energy sources such as solar energy and wind energy are unstable and intermittent during generation. The utilization rate and stability of renewable energy can be improved by combining certain energy storage and generating systems [4]. The hybrid system comprising photovoltaic cells, an electrolyzer, and a PEMFC harnesses solar power to operate the electrolyzer and produce hydrogen. The hydrogen is then compressed and stored in a storage tank, which is connected to the fuel cell for electricity generation. This setup effectively mitigates the intermittency of solar power production, thereby providing a more consistent and reliable source of energy. This hybrid system is completely clean energy system with no greenhouse gas emissions. Moreover, the costs associated with the fuel cell and electrolyzer components are expected to become more appealing in the future [5]. Based on the aforementioned advantages, the study focuses on the PEMFC. The subsequent section provides a detailed discussion on the working principle and components of the PEMFC.

PEMFC mainly consumes hydrogen as fuel and oxygen/air as oxidizer. The primary products of this reaction are water and heat. PEMFC consists of Proton Exchange Membrane (PEM), Catalyst Layer (CL), Gas Diffusion Layer (GDL), and Current Collectors (CCs). Flow field are engravings on current collectors on both anode and cathode. Flow field facilitate reactants to catalyst sites through GDL. Simultaneously, formed water at the cathode catalyst was transferred to the flow field via GDL through capillary action[6]. Flow field collects the water and drive them out due to the pressure difference in them.

Among the various studies on PEMFCs, flow field design is considered as a primary factor that affects the performance significantly. Not only in PEMFCs, flow field design influence can be observed in other fuel cells also [7-9].Various novel designs were developed by the researchers in order address the performance issues due to water and heat management.

Initially, pin and parallel flow fields were widely used due to their a simplicity, but later it was found to be ineffective in distributing species[10,11]. Subsequent improvements resulted in more efficient designs such as serpentine, interdigitated, and bio-inspired flow fields[12-14]. Compared to parallel and pin flow fields, these designs exhibited higher pressure drops. Pressure drop helps in distribution of reactants and purging of water in serpentine and interdigitated [15]. However, this can result in significant parasitic losses, which should be taken into account during optimization. Hence, single serpentine flow field was further modified into double, triple and multiple parallel serpentines in order to reduce the pressure drop, but led to decrease in power density [16].

In similar lines, interdigitated showed higher pressure drop than single serpentine[17,18]. Despite the higher pressure drop, interdigitated flow fields showed three times more power density than serpentine designs [19]. Due to their good distribution of species properties and drivability of product water, the researchers have developed modified interdigitated designs such as diagonal and spiral interdigitated, to reduce the pressure drop [20].

An efficient flow field must have uniform distribution of membrane water content, current, and temperature while also being capable of evacuation of product water with little pressure loss [14]. Additionally, it should reduce water flooding and enhance proton conductivity to improve the consumption of reactants [21,22].Significantly, water management is a critical problem in PEMFCs, which hinders the performance [23].

Apart from the above flow fields, multiple studies have been conducted to assess the characteristics of different flow fields such as Lung, Leaf, Zigzag, and Sinusoidal using both experimental and computational fluid dynamic (CFD) analysis [24,14,13,25])[26]. The CFD analysis yielded similar results to experimental studies, indicating the reliability of numerical models in scrutinizing electrochemical performance. This approach saves time and cost compared to experimentation[27,3,28]. Various researchers used CFD solvers to evaluate the performance of PEM fuel cells, and the results are in good agreement with the physics.

This article presents a novel and innovative approach by introducing the L-serpentine design as a modification to the conventional single serpentine design. The novelty lies in its objective to increase oxygen consumption while simultaneously reducing the travel length of product water for rapid evacuation. Additionally, compared to the interdigitated design, the L-serpentine design offers advantages such as lower pressure drop improved driving capability, and elimination of blind spots. Through comprehensive CFD analysis, this study focuses on enhancing water and thermal management to optimize fuel cell performance. This novel design

concept and its potential to improve fuel cell efficiency make this research a significant contribution to the field.

## 2. Methodology

### 2.1. Model development

For the current analysis, a small active area of 21mm x 21mm was chosen, as shown in figure 1 with layouts of Single Serpentine Flow Field (SSFF) on the left and L-Serpentine Flow Field (LSFF) on the right. The reasons for choosing small active are:i) large area minimizes the focus on the flow field; ii) a small active area/domain reduces the computational load. Furthermore, sharp edges at the turnings were considered to reduce computational load, though round or curved edges performs better. However, similarity for edges been considered in both designs[29].All the inlet parameters were calculated as required for the active area. The main idea of the current work is to enhance the contact time of the reactants against the products, which doesn't require much time to evacuate. In view of the above, a LSFF was considered as it also avoids flooding in the channel.

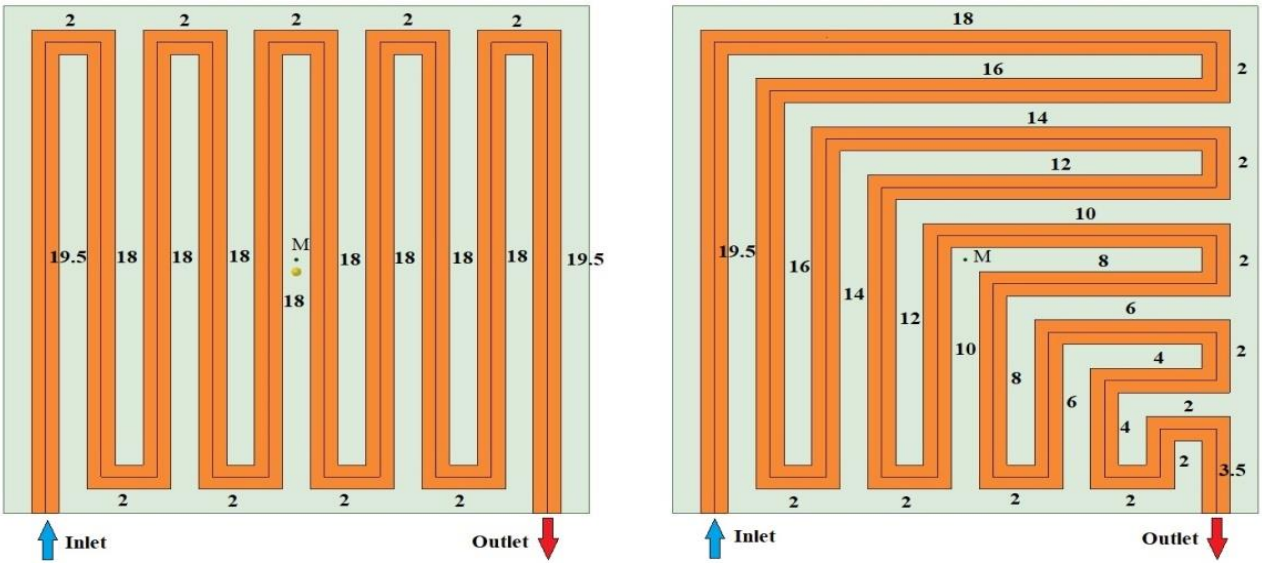


**Figure 1. SSFF (left) LSFF (right).**

Figure1shows the average length in mm, and a center line is drawn in the channels to measure total length. Both flow fields measured 201 mm and length is indicated at top, bottom, and sides, respectively. Other dimensions were kept constant and they are given in table 1.

**Table 1. Dimensions for the model.**

| | Dimension (mm) | Ref. |
|---|---|---|
| Membrane area | 21x21 | [11] [30] |
| Electrolyte thickness | 0.178 | [31] [30] |
| Gas Diffusion Layer (GDL) thickness | 0.25 | |
| Catalyst Layer (CL) thickness | 0.02 | |
| Channel width | 1 | [31] |
| Channel height | 1 | |
| Current collector (CC) thickness | 2 | |
| Rid width | 1 | |

In LSFF, from the midpoint to outlet, the length has been reduced by 40% approximately (where M indicates midpoint) compared to SSFF.

Inlet and outlets are indicated with arrows, as shown in figure1; in all the subsequent sections, same notation has been followed for both anode and cathode flow fields.

### 2.2. Governing equations

Governing equations including conservation of mass (Equation 11), momentum (Equation 13), energy (Equation 16), and species transport (Equation 19) were considered [32,33]. To solve the electro-chemistry, Ansys FLUENT uses two potential equations to solve electron transfer (Equation 1) and protons transfer (Equation 2). Electrons transfer equation applicable for catalyst and current collector regions, whereas protons transfer equation applicable within the membrane region.

$$\nabla.(\sigma_{sol}\nabla\emptyset_{sol}) = R_{sol} \quad (1)$$

$$\nabla.(\sigma_{mem}\nabla\emptyset_{mem}) = R_{mem} \quad (2)$$

The source terms $R_{sol}$ and $R_{mem}$are calculated by using Buttler-Volmer equations (Equation 3) and (Equation 4),whereas $R_a$ and $R_c$ are exchange current densities calculated at anode and cathode side for both solid and membrane phases.

$$\mathbf{R_a} = \mathbf{I_a^{ref}}\left(\frac{[H_2]}{[H_2]_{ref}}\right)^{\gamma a}\left[\exp\left(\frac{\alpha_a^a F\eta_a}{RT}\right) - \exp\left(-\frac{\alpha_c^a F\eta_a}{RT}\right)\right] \quad (3)$$

$$\mathbf{R_c} = \mathbf{I_c^{ref}}\left(\frac{[O_2]}{[O_2]_{ref}}\right)^{\gamma c}\left[-\exp\left(\frac{\alpha_a^c F\eta_c}{RT}\right) + \exp\left(-\frac{\alpha_c^c F\eta_c}{RT}\right)\right] \quad (4)$$

Membrane conductivity ($\sigma_{mem}$) is found by equation (Equation 5), this equation again depends on the operating temperature and membrane water content($\lambda$) (Equation 6).

$$\sigma_{mem} = (0.00514\lambda - 0.00326) * \exp\left(1268\left(\frac{1}{303} - \frac{1}{T}\right)\right) \quad (5)$$

$$\lambda = \begin{cases} 0.043 + 17.81a - 39.84a^2 + 36a^3, \\ (a < 1) \\ 14 + 1.4(a-1), \\ (a > 1) \end{cases} \quad (6)$$

Water activity(a) is calculated by (Equation 7),

$$a = \frac{X_w P}{p^{sat}} \quad (7)$$

where $X_w$is mole fraction of water,Pis operating pressure, and$p^{sat}$ is saturation pressure.
Activation losses at anode ($\eta_a$) and cathode ($\eta_c$)are found by (Equation 8) and (Equation 9), respectively.

$$\eta_a = \phi_{sol} - \phi_{mem} \quad (8)$$

$$\eta_c = \phi_{sol} - \phi_{mem} - V_o \quad (9)$$

Open circuit potential ($V_o$) was considered as function of temperature (Equation 10).

$$V_o = 0.0025T + 0.2329 \quad (10)$$

**Conservation of mass** (Equation 11)

$$\nabla.(\rho\varepsilon V) = S_m \quad (11)$$

The source terms($S_m$) changes according to location (Equation 12).

$$\left.\begin{array}{c} S_m = 0, \\ \text{for flow fields, GDLs} \end{array}\right| \begin{array}{c} S_{ma} = -\frac{MW_{H_2}}{2F} i_a \\ S_{mc} = \frac{MW_{H_2O}}{2F} i_c - \frac{MW_{O_2}}{4F} i_c \\ \text{For CLs} \end{array} \quad (12)$$

**Conservation of Momentum** (Equation 13)

$$\nabla.(\rho\varepsilon VV) = -\nabla P + \nabla\tau + S_p \quad (13)$$

Shear stress (Eq.14)different in various regions due to the effect of porosity, porosity brings additional source terms (Equation 15) in porous regions.

$$\nabla\tau = \begin{cases} \mu\nabla^2 V; \\ \text{for Flow fields} \\ \mu\nabla^2 V + 2.25\frac{(1-\varepsilon)^2}{\varepsilon^2}\mu\nabla^2 V - \frac{\varepsilon\mu}{k_p}V; \\ \text{for porus media} \end{cases} \quad (14)$$

$$S_p = 0 \text{ for flow fields}; \quad S_p = -\left(\frac{\mu}{k_p}\right)V \text{ for porous media} \quad (15)$$

**Conservation of Energy** (Equation 16)

$$\nabla.\left(V\left(\rho\varepsilon c_p T\right)\right) = \nabla.(k_{eff}\nabla T) + S_e \quad (16)$$

Effective conductivity (Equation 17) can be considered as fluid conductivity in flow fields, whereas in porous media porosity and conductivity of solids and fluids were considered.

$$k_{eff}\begin{cases} k_f \text{ for FFs} \\ -2k_s + \left(\frac{\varepsilon}{2k_s + k_f} + \frac{1-\varepsilon}{3k_s}\right)^{-1} \\ \text{for porus media} \end{cases} \quad (17)$$

Energy source term (Equation 18) is obtained by combining heats generated through ohmic losses ($i^2R_{ohm}$), heat of reaction ($h_{reaction}$), current conduction heat($\eta R_{a,c}$), and phase change from liquid to vapour ($h_{phase}$).

$$S_e = i^2 R_{ohm} + h_{reaction} + \eta R_{a,c} + h_{phase} \quad (18)$$

**Species transport** (Equation 19)

$$\nabla.(\rho\varepsilon V y_i) = -\nabla.\left(\rho(D_i\nabla.y_i)\right) + S_s \quad (19)$$

Stephen Maxwell formulation helps to calculate the diffusive coefficient of the species (Equation 20) is used,which also considers tortuosity of gas diffusion.

$$D_i = \varepsilon^{1.5} D_i^o \left(\frac{P_0}{P}\right)\left(\frac{T}{T_0}\right)^{3/2} \quad (20)$$

$$S_{H_2} = -\frac{MW_{H_2}}{2F}R_a; \quad S_{O_2} = -\frac{MW_{O_2}}{2F}R_c; \quad S_{H_2O} = -\frac{MW_{H_2O}}{2F}R_c \quad (21)$$

### 2.3. ANSYS fluent setup

An ANSYS-fluent add-on module for fuel cell analysis was considered for the study. Flow was assumed as steady, isothermal, isotropic, incompressible, and multiphase models were taken into account. Velocity at anode and cathode inlet calculations were considered from Nguyen et.al study (Equations 22 and 23) [34]. These velocities turned into mass flow rates by multiplying them with specific volumes (mass flow rates given in table 2). Voltage ranging from

0.4 to 0.9V was applied only at the cathode current collector terminal.

All the equations are solved individually by the solver, and they are combined using SIMPLE solver. Subsequently, the relevant equations were discretized using the second-order upwind scheme for better accuracy. Solution controls were applied for momentum (0.3) and pressure (0.7). BiConjugate Gradient STABilization method (BCGSTAB) was employed for anode and cathode potential stabilization methods along with F-cycle method to enhance the convergence speed. Advanced solution controls for potentials were set to 0.0001. All residuals were set to $10^{-8}$.Additionally, a convergence criterion $10^{-6}$ was used for output current density[35][32]. Parameters and boundary conditions are tabulated below in table 2.

$$u_{a,in} = \zeta_a \frac{I_{ref}}{2F} \frac{RT}{P} \frac{A_{active}}{A_{ff}} \frac{1}{X_{H_2}} \quad (22)$$

$$u_{c,in} = \zeta_c \frac{I_{ref}}{4F} \frac{RT}{P} \frac{A_{active}}{A_{ff}} \frac{1}{X_{O_2}} \quad (23)$$

**Table 2. Parameters and boundary conditions for the model.**

| Parameter | | Anode | | Cathode | Ref. |
|---|---|---|---|---|---|
| Stoichiometry | $\zeta_a$ | 2 | $\zeta_c$ | 2 | |
| Reference current density | $I_{ref}$ | 10,000 A/m$^2$ | $I_{ref}$ | 10,000 A/m$^2$ | |
| Humidifying temperature | $T$ | 60, 70, 80$^0$C | $T$ | 60, 70, 80 $^0$C | |
| Pressure | $P$ | 3 atms | $P$ | 3 atms | |
| Relative humidity | $RH$ | 100% | $RH$ | 100% | |
| Voltage | | 0 | | 0.4 – 0.9 V | |
| Concentration exponents | $\gamma_a$ | 0.5 | $\gamma_c$ | 1 | [36][30] |
| Exchange coefficients | $\alpha^a_{a'}$ $\alpha^a_c$ | 0.5 | $\alpha^c_{a'}$ $\alpha^c_c$ | 2 | |
| Active area | $A_{active}$ | 21x21 mm$^2$ | $A_{active}$ | 21x21 mm$^2$ | |
| Area of cross section of flow field | $A_{ff}$ | 1x1 mm$^2$ | $A_{ff}$ | 1x1 mm$^2$ | |
| Hydrogen mole fraction | $X_{H_2}$ | 0.897 | - | - | |
| Oxygen mole fraction | - | - | $X_{O_2}$ | 0.1885 | |
| Gas diffusion layer porosity | | 0.7 | | 0.7 | [37] |
| Catalyst layer porosity | | 0.38 | | 0.38 | |

## 2.4. Grid independence study

A grid independence study for the models is shown in table 3, and current density was measured at 0.6 V for different element sizes of LSFF. All the dimensions and parameters were considered as per table 1 and table 2. As indicated in the table 3, elements considered for the numerical study were increased from 1 million to 2.5 million approximately. A percentage deviation of less than 1% with respect to current density occurred for 0.6 million elements was observed.

**Table 3. Grid independence study.**

| Elements | Current density (A/cm$^2$) | % deviation |
|---|---|---|
| 97,020 | 0.758 | |
| 388,080 | 0.7766 | 2.457 |
| 606,375 | 0.7831 | 0.838 |
| 2,425,500 | 0.7891 | 0.761 |

## 2.5. Validation

The validation for this study was taken from Lin Wang, experimental results for input conditions at 70$^0$C and 3 atm[36]. A single serpentine flow field with an active area 72x72mm$^2$ considered. Keeping the other dimensions mentioned in table 1. Mass flow rates and mass fractions of reactants were calculated in accordance with active area membrane.

The variation of voltage with current density as observed in figure2, as observed from the graph the numerical variation well justifies the experimental study. However, a minimum deviation was observed, the reasons being the variation in water formation is higher at higher current densities, which is more precise in experiments due to multiphase in nature.

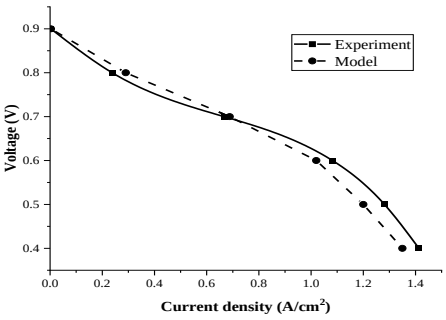


**Figure 2. Experimental and numerical validations.**

With simulations other approximations like square cross section, sharp edges flow fields, and adiabatic conditions at the current collectors affected the output current density.

## 3. Results and discussion

### 3.1. V-I and P-I characteristics

In figures 3 and 4, it is evident that as the temperature increases, the current density and power density also increase. Both the LSFF and SSFF flow fields show a similar trend, with the current density initially being minimum for lower voltages and gradually increasing as the voltage level drops. However, at higher temperatures, the LS80 exhibits a higher current density compared

to the SS80. Similarly, the power density follows the same trend, with the LSFF model outperforming the SSFF model at higher temperatures within the same voltage range. At higher voltages, the variation in current density and power density becomes insignificant.

Numerical analysis was conducted on the considered models, spanning a temperature range of 60 – 80$^0$C, with 3 atm pressure as part of the study. The temperature range aimed to assess the effectiveness of the modified design. It is worth mentioning that the performance was less satisfactory at 60$^0$C due to sluggish reaction kinetics at lower temperatures. As the temperature increased beyond that point, the performance improved. The highest power and current densities were observed at 80$^0$C within this range. However, operating above 80$^0$C was not recommended due to several factors. These include potential membrane degradation, increased water loss through evaporation, enhanced electrode corrosion (which is directly proportional to temperature), and consequent increase in ohmic losses. Although performance generally improves with temperature, operating at high temperatures can negatively affect membrane conductivity [38,39]. To strike a balance, the optimum temperature for further analysis was determined to 70$^0$C.

The values of maximum power densities are observed at 0.6 V at different temperatures from the graphs shown in figure 4. The following characteristics were chosen for obvious reasons: i) Thermal (Temperature contours) ii) Flow (Pressure, Streamline contours) iii) species ($H_2O$, $O_2$ species contours) iv) Electric (V-I and P-I characteristics). All the contours in the subsequent sections are drawn at 70$^0$C and 0.6 V.

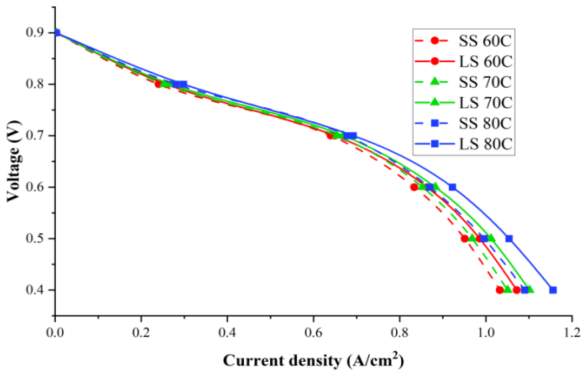


**Figure 3. Voltage *vs.*current density.**

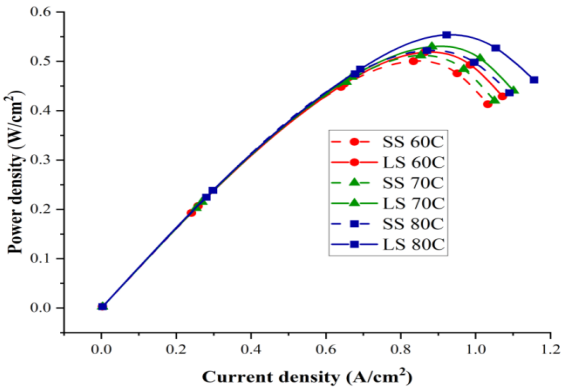


**Figure 4. Power density *vs.*current density.**

### 3.2. Thermal characteristics

The temperature contours shown in figure 5 were plotted at the cathode GDL and CL interface. Temperature rise is more considerable on the cathode side than anode side [34].The temperature rises in new design, i.e. LSFF, is only 2$^0$C, but in traditional SSFF rise was 14$^0$Cand subsequently the rise in SSFF was mainly confined to the initial active area. In contrast, LSFF design displays a mostly uniform temperature rise.

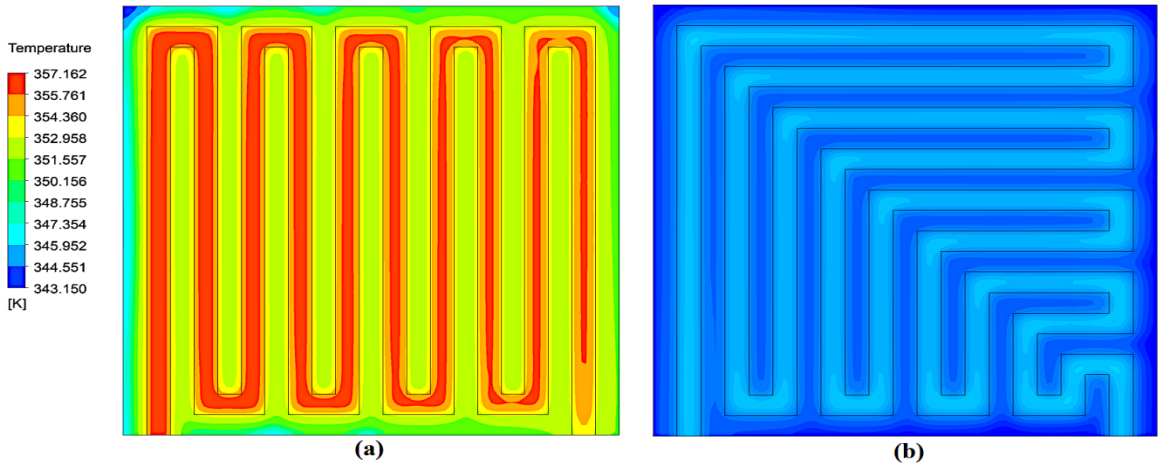


**Figure 5. Temperature contours for SSFF and LSFF.**

From the same figure 5 it can be inferred that the sudden U-bend turn in SSFF gives rise to sudden drop in velocity of the reactants, thereby increased resident time at the U-bends. Hence temperature

rise observed in the initial phase, whereas in LSFC, due to the adoption on L-shape bends along with U-bends, it reduces the sudden velocity drop at L-bends compared to U-bends. Though the numbers of U-bends are same in both the designs, LSFC allows the species to spread throughout due to L-bends.

Furthermore, in SSFF, the temperature rise decreased in the later phase. This is due to the formation of water or accumulation of water at the end phase (which can be observed in $H_2O$ mass fraction and MWC sections). The water formed absorbs the thermal energy thus reflected in the reduced temperature. However, in case of LSFF, the time available for products in flow channel was reduced. Furthermore, increasing in temperature decreases the condensation and decreases the moisture content [40], this has dried up the flow field area in SSFF which can be noticed from figure 10. Hence, LSFF design solves thermal management problem in the flow field. Moreover, constant temperature reduces thermal stresses in current collectors [41,42].

Temperature rise at each voltage is been plotted in the figure 6 bar chart. At higher voltages the rise in temperature is almost similar in the both designs. At lower voltages, the rise in temperature is significant which corresponding to higher current density production, thus higher reactions happening in the cell produces higher temperature. Interestingly, the higher temperature of an LSFC is nearly identical for all voltage processes, making it an excellent design by eliminating exterior cooling without fluctuating heat burden. Notably, the temperature increase at each voltage in SSFF is greater than in LSFF. As previously stated, similar causes for higher temperatures can be extrapolated.

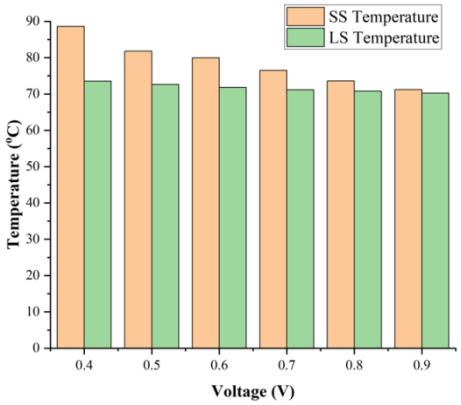


**Figure 6. Maximum temperature attained at each voltage.**

### 3.3. Pressure drop in cathode channels

The volume rendering method in Ansys post processing is used to calculate pressure drop in cathode channels.

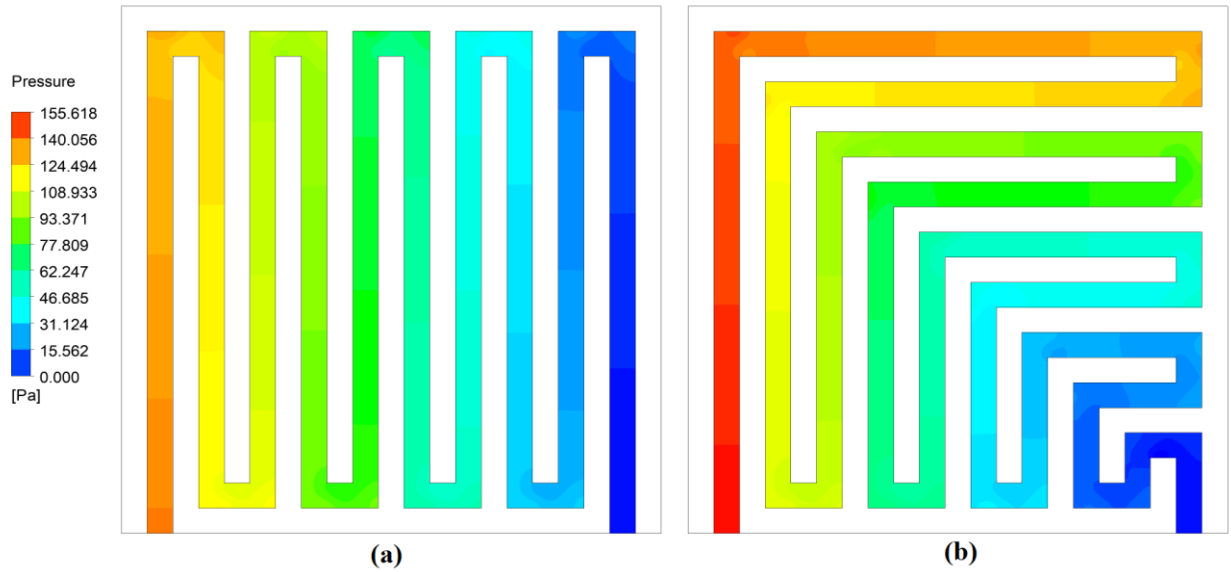


**Figure 7. Pressure drop in cathode channels of SSFF and LSFF.**

It is apparent from figure 7 that the pressure drop in the LSFF was higher as compared to SSFF. However, the percentage of pressure drops in the flow fields with respect to inlet pressure of 3 atm was 0.0464% and 0.051%, respectively. This corresponds to 14 Pa higher inlet pressure requirements for LSFF.

The majority of new designs have a significant pressure drop, which is undesirable since it causes parasitic power losses. However, pressure drop is responsible for improved resident time of

reactants in the flow field [43]. As a result, the temperature at the corners and U-bends rose sharply which can be observed in the preceding section (Temperature).

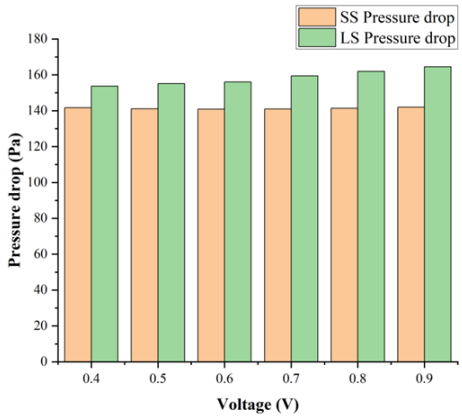


**Figure 8. Pressure drop *vs.* voltage.**

Pressure drop in SSFF remained almost constant, Whereas, in LSFF pressure increased slightly as the voltage increased.

### 3.4. Streamline contours

The streamline contours shown in figure 9 are plotted for cathode channels. The primary objective of these contours was to evaluate the occurrence of eddies at the sharp edges. After analyzing the contours, it becomes clear that the influence of secondary flows (indicated in figure 9 as circles) on sharp edges is insignificant, resulting in a decreased turbulence effect. Initially, there were small secondary flows observed at the corners in the initial turns due to high velocity, but later these flows diminished. The decision to incorporate sharp edges was made in order to reduce the computational load. If curved edges had been considered instead, small secondary flows would have been eliminated. The velocity distribution in the both channels seems uniform; the uniform velocity distribution of the reactants at the flow channel avoids parasitic current may be occurring due to potential difference [41].

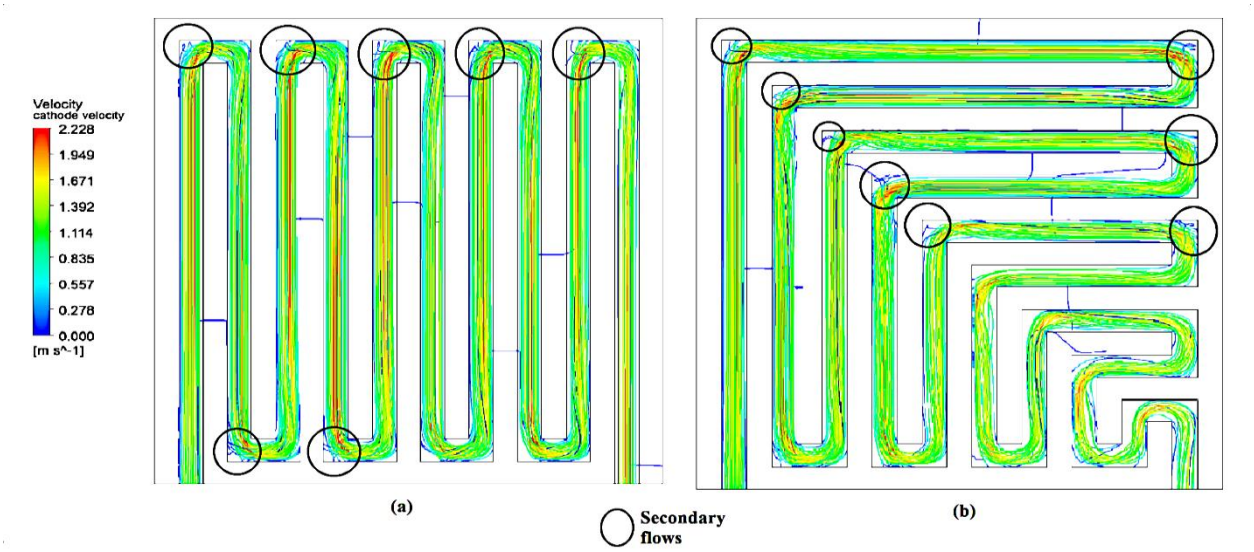


**Figure 9. Cathode channel streamline contours.**

### 3.5. Membrane water content

The outlines shown in figure 10 were drawn at the membrane and CL on cathode side interfaces since product water originates from the reactions at cathode end. The other reasons for water in the membrane are electro-osmotic drag and reverse diffusion [44]. The change in membrane water concentration (MWC) of SSFF is minimal, hovering around 14, whereas, for LSFF it increased from 14 to 15.45 (within the limits of range 14 to 22). Notably, if MWC > 14, then the membrane is fully saturated with water, which allows both water molecules and $H_3O+$ ions to move freely and easily through the membrane. This is the most desirable regime for PEMFCs, as it maximizes the proton conductivity and enhances the overall performance of the fuel cell [38].

Distribution of MWC in LSFF is more uniform than SSFF. In SSFF, due to higher temperatures in the initial phase has dried up the membrane. From figure 10 in SSFC, water is initially driven and accumulates towards the end due to the pressure difference, which is higher in the initial stages but reduces later on. This pressure difference drives the water content. On the other hand, LSFC experiences a higher pressure drop in overall, but the sudden pressure drop at U-bend is reduced. Additionally, LSFC requires less pressure to remove product water near the outlet. Due to

much available MWC, proton conductivity increased and led to increased power. In addition, this even distribution of MWC reduced hot spots, which extends the lifespan of the membrane [45]. The ability of water evacuation can be observed in the next section.

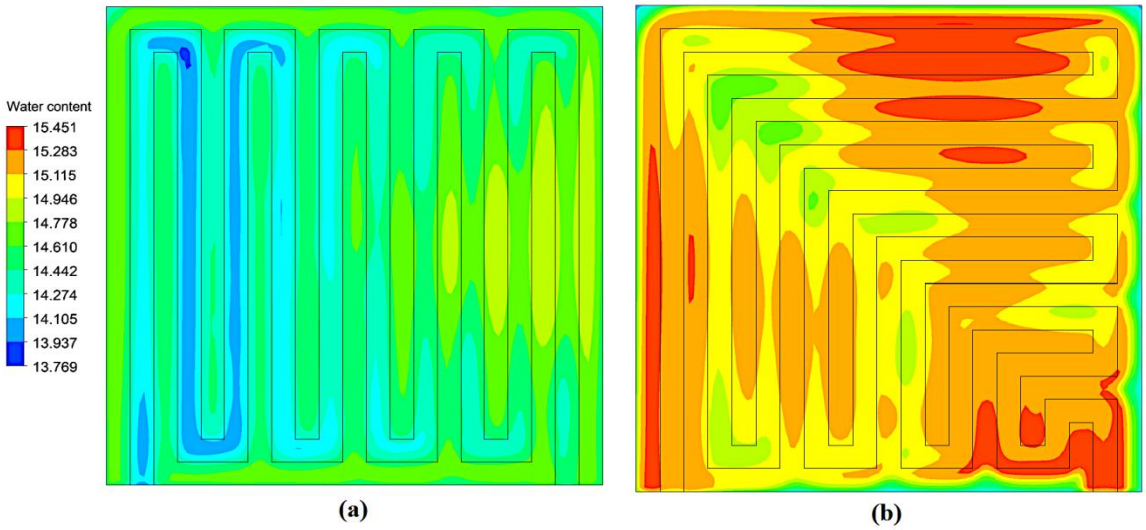


**Figure 10. Membrane water content at cathode side GDL and CL interface.**

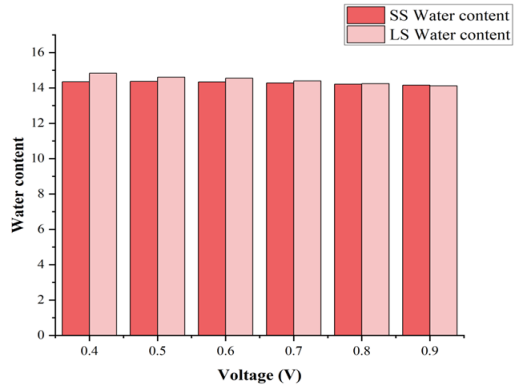


**Figure 11. Average membrane water content *vs.* voltage.**

Figure 11 depicts the average surface water content of the membrane with respect to voltage. It was observed that the average water content is the same at higher voltages, but increases at lower voltage. Lower voltage (higher current) leads to the production of more amount of water.

### 3.6. $H_2O$ mass fraction

To determine the $H_2O$ mass fraction, a mid plane in the cathode channel was used. In figure 12, the contours show that in SSFF, $H_2O$ mass fraction was increased from an input value of 0.066 to 0.112, whereas it is increased to 0.087 only in LSFF.

The increase in $H_2O$ mass fraction demonstrates that $H_2O$ has generated from the reactions and is increasing towards the channel's end. The buildup of $H_2O$ in SSFF caused a drastic increase in mass fraction, but accumulation in LSFF was minimized due to shorter end phases. In contract, more $H_2O$ indicates more reactions, but the less $H_2O$ in LSFC can justified by observing MWC (Figure 10). These contours are co-related, MWC indicates how much water is produced during reactions and $H_2O$ mass fraction tells the amount water at various locations. Hence, MWC of LSFC is higher ie. Membrane more humid compared SSFC design. Though equal amount of humidity provided at the inlet. Therefore, LSFC showed better membrane wetability and better water evacuation. Furthermore, LSFF assured improved removal of water content from the channels by 22.3% (22% approximately), which implicates a critical concern in the design of fuel cell flow channels.

### 3.7. $O_2$ mass fraction

The contours in figure 13 were plotted on a mid plane created at the cathode channel. The range of $O_2$ mass fraction reduction in SSFF is less as compared to LSFF. The minimum mass fractions obtained at the outlet are 0.128 and 0.118 for SSFF and LSFF, respectively.

$O_2$ mass fraction contours clearly justify $H_2O$ mass fraction contours. LSFF has reduced oxygen mass fraction, indicating more consumption [47]. The modified designed allowed an increase in oxygen's resident time in the initial phase. As a result, LSFF outperformed SSFF in terms of reactant use by 7.8% (approximately 8%). In both configurations, the decrease in $H_2$ mass fraction was small. Furthermore, the high dissociation energy of oxygen received the greatest attention in the literature too.

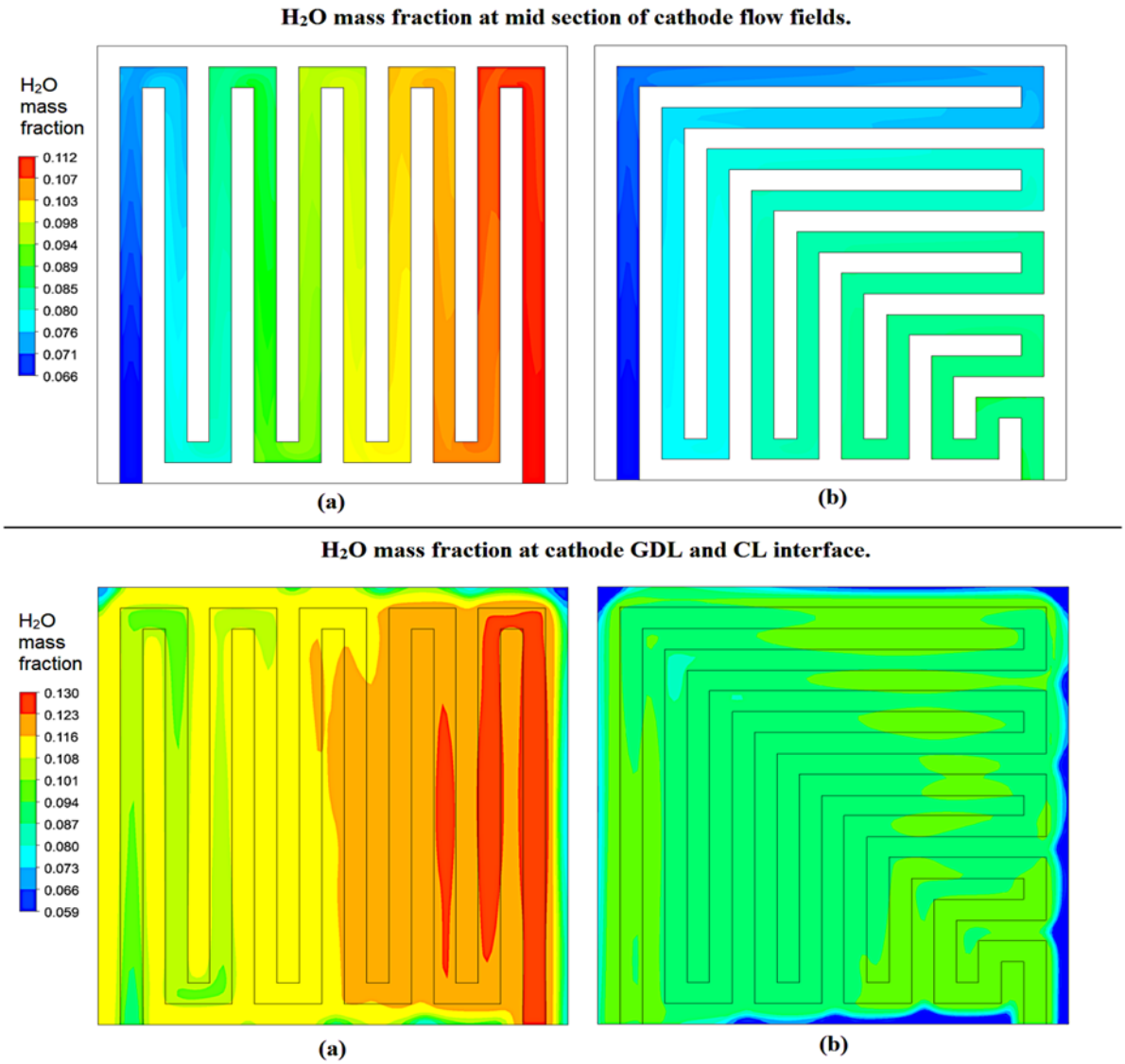


**Figure 12. Cathode channel $H_2O$ mass fraction contours.**

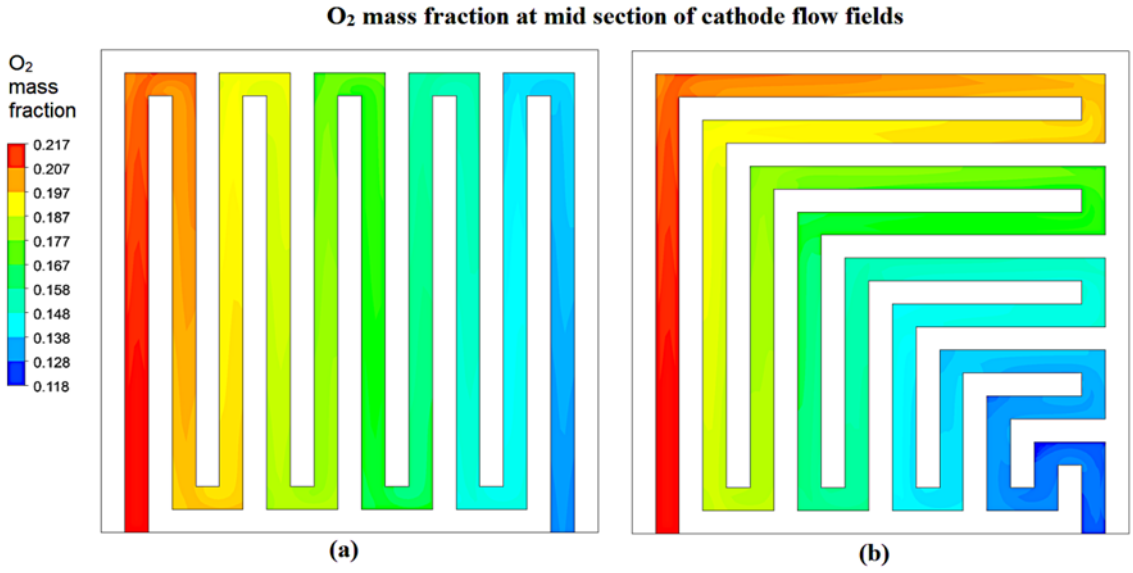

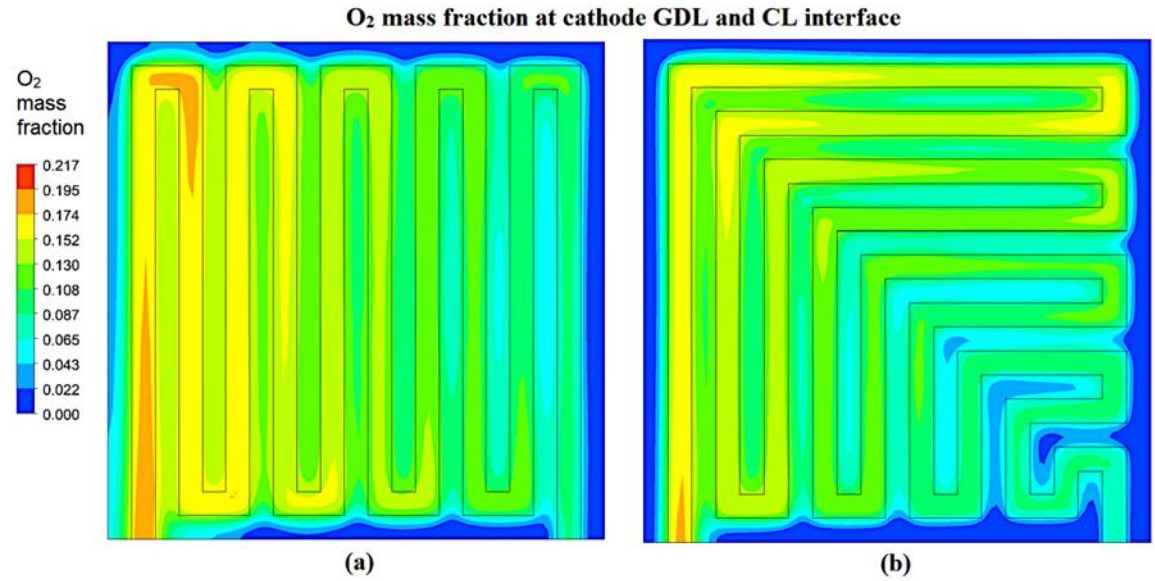


**Figure 13. $O_2$ mass fraction in cathode channels.**

### 3.8. VI and PI characteristic curve

The Overall performance of a fuel cell was evaluated using VI and PI curves. The graph in figure 14 was drawn for 70 $^0$C and 3 atm pressure operating condition. It is very clear that LSFF current density or power density is higher compared to SSFF. The maximum current and power densities were given in table 4. At maximum power density, a 10% (approximately) rise was observed.

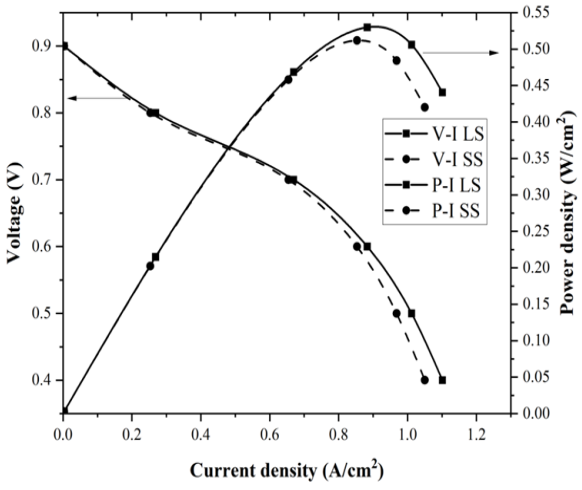


**Figure 14. V-I and P-I characteristic curves.**

VI characteristic curves emphasizes the various losses. The losses are activation losses, ohmic losses and concentration losses. The modified design showed similar activation losses, since these losses are more dependent on catalyst. Ohmic losses found to be decreased because increased membrane content. Furthermore, concentration losses were reduced by increased the current density, since the efficient product water evacuation helps the fresh reactant to reach the active site. Hence, polarization losses or the over-voltages were reduced with L-sepentine.

**Table 4. Maximum current and power densities at 0.6 V.**

| Flow field | Current density (A/cm$^2$) | Power density (W/cm$^2$) | % rise |
|---|---|---|---|
| **SSFF** | 0.7132 | 0.42792 | |
| **LSFF** | 0.783 | 0.4698 | 9.787 |

### 4. Conclusions

The comprehensive numerical study of the innovative L-Serpentine flow field (LSFF) design compared to the standard single serpentine flow field (SSFF) design has yielded remarkable conclusions. By adopting the LSFF, significant enhancements in performance have been achieved, addressing key challenges related to thermal management and water distribution within the fuel cell.

The findings highlight the following compelling conclusions from the LSFF-SSFF comparison:

1. The incorporation of LSFF design effectively reduces the travel length for products by an impressive 40%, resulting in accelerated evacuation from the fuel cell.
2. Remarkably, the LSFF design demonstrates minimal temperature rise and achieves near-uniform temperature distribution, alleviating thermal stresses on current collectors and bipolar plates.
3. While LSFF shows a slightly higher pressure drop, requiring an additional 14 Pa of pressure, its impact on power density remains

negligible, making it an attractive choice for fuel cell applications.

4. The LSFF design showcases improved consumption of oxygen ($O_2$) and more efficient removal of water ($H_2O$) at the cathode end. This translates to an impressive 8% increase in $O_2$ consumption and a remarkable 22% enhancement in $H_2O$ removal.
5. Both the V-I (voltage-current) and P-I (power-current) characteristic curves demonstrate significant improvements in current density and power density outputs. The modified LSFF design exhibits an impressive 10% increase in both current density and power density.

Therefore, the LSFF design emerges as a highly promising solution for overcoming thermal and water management challenges in fuel cells. Further exploration should include investigations into the benefits of rounded edges to reduce pressure drop in flow fields, as well as the effects of larger active areas under various inlet conditions. These advancements hold tremendous potential for future studies in fuel cell technology.

## 5. Abbreviations

| | |
|---|---|
| **PEMFCs** | Proton Exchange Membrane Fuel cells |
| **SSFF** | Single Serpentine Flow Field |
| **LSFF** | L-Serpentine Flow Field |
| **GDL** | Gas Diffusion Layer |
| **MWC** | Membrane Water Content |
| **RH** | Relative Humidity |
| **BCGSTAB** | Bi-Conjugate Gradient STABilizion |
| **SIMPLE** | Semi-Implicit Method for Pressure Linked Equations |
| **CL** | Catalyst Layer |

## 6. Nomenclature

| | |
|---|---|
| $\sigma_{sol}, \sigma_{mem}$ | Ionic conductivity in solid and membrane |
| $\emptyset_{sol}, \emptyset_{mem}$ | Potential of the cell in solid and membrane |
| $R_{sol}, R_{mem}$ | Conductive current (A/m$^2$) |
| $R_{a,c}$ | Volume exchange current density at anode and cathode |
| $I_{a,c}^{ref}$ | Reference exchange current density at anode, cathode (A/m$^2$) |
| $\gamma_{a,c}$ | Concentration exponent |
| $\eta_{a,c}$ | Activation losses at anode, cathode |
| $[H_2], [O_2]$ | Concentration of species |
| $\alpha_a^a$ | Anodic transfer coefficient at anode |
| $\alpha_c^a$ | Cathodic transfer coefficient at anode |
| $\alpha_a^c$ | Anodic transfer coefficient at cathode |
| $\alpha_c^c$ | Cathodic transfer coefficient at cathode |
| $\lambda$ | Membrane water content |
| $a$ | Water activity |
| $X_w$ | Water vapour fraction |
| $p^{sat}$ | Saturation pressure |
| $\eta_{a,c}$ | Activation losses at anode, cathode |
| $V_o$ | Open circuit voltage (V) |
| $\rho$ | Density of fluid |
| $V$ | Velocity vector |
| $\varepsilon$ | Porosity |
| $S_m$ | Mass source term |
| $MW$ | Species molecular weight (kg/mol) |
| $i_{a,c}$ | Anode and cathode current density (A/m$^2$) |
| $\tau$ | Viscous shear stress tensor (N/m$^2$) |
| $S_p$ | Source term due to porous media |
| $\mu$ | Viscosity of fluid |
| $k_p$ | Permeability of porous media |
| $k_{eff}$ | Effective thermal conductivity (W/m$^2$K) |
| $k_f$ | Thermal conductivity of fluid (W/m$^2$K) |
| $k_s$ | Thermal conductivity of Solid (W/m$^2$K) |
| $R_{ohm}$ | Ohmic resistance |
| $y_i$ | Mass fraction of the species |
| $D_i$ | Mass diffusion coefficient |
| $D_i^o$ | Mass diffusion coefficient at standard conditions |
| $S_s$ | Species source term |
| $T_E$ | Electrolyte thickness |
| $T_G$ | Gas diffusion layer thickness |
| $T_C$ | Catalyst layer thickness |
| **W** | Channel width |
| **H** | Channel height |
| $C_T$ | Current collector thickness |
| **R** | Rid width |
| $u_{a,in}$ ; $u_{c,in}$ | Inlet velocities of reactant (m/s) |
| $\zeta_a$; $\zeta_c$ | Stoichiometry ratio |
| $I_{ref}$ | Reference current density (A/m$^2$) |

| | |
|---|---|
| $F$ | Faradays constant (96485 C/mol) |
| $R$ | Ideal gas constant (8.314 J/mol.K) |
| $P$ | Pressure (Pa) |
| $T$ | Temperature (K) |
| $A_{active}$ | Active area of the fuel cell ($m^2$) |
| $A_{ff}$ | Area of cross section of flow field ($m^2$) |
| $X_{H_2}; X_{O_2}$ | Mole fraction of hydrogen and oxygen |

## 7. References


[1] A. Garai and D. K. Pandey, 2022, "EPRA International Journal of Research and Development ( IJRD ) Role of renewable energy for clean energy transition plan for india and determination of retariff under cerc terms and conditions of resources regulations , 2020 EPRA International Journal of," Vol. 7838, No. July, pp. 51–56.

[2] I. Dincer and C. Acar, 2014, "Review and evaluation of hydrogen production methods for better sustainability," Int. J. Hydrogen Energy, Vol. 40, No. 34, pp. 11094–11111, doi: 10.1016/j.ijhydene.2014.12.035.

[3] S. Mohanty, A. N. Desai, S. Singh, V. Ramadesigan, and S. M, 2021, "Effects of the membrane thickness and ionomer volume fraction on the performance of PEMFC with U-shaped serpentine channel," Int. J. Hydrogen Energy, Vol. 46, No. 39, pp. 20650–20663, doi: 10.1016/j.ijhydene.2021.03.252.

[4] Z. Zhang, S. Wu, H. Miao, and T. Zhang, 2022, "Numerical Investigation of Flow Channel Design and Tapered Slope Effects on PEM Fuel Cell Performance," Sustain., Vol. 14, No. 18, doi: 10.3390/su141811167.

[5] M. Shaygan, M. A. Ehyaei, A. Ahmadi, M. E. H. Assad, and J. L. Silveira, 2019, "Energy, exergy, advanced exergy and economic analyses of hybrid polymer electrolyte membrane (PEM) fuel cell and photovoltaic cells to produce hydrogen and electricity," J. Clean. Prod., Vol. 234, pp. 1082–1093, doi: 10.1016/j.jclepro.2019.06.298.

[6] I. Korkischko, B. S. Carmo, and F. C. Fonseca, 2017, "Shape Optimization of PEMFC Flow-channel Cross-Sections," Fuel Cells, Vol. 17, No. 6, pp. 809–815, doi: 10.1002/FUCE.201700168.

[7] R. Kumar, A. V. Babu, and S. H. Sonawane, 2022, "Numerical investigation of a novel rhombohedral interconnector configuration for planar solid oxide fuel cells," Int. J. Green Energy, Vol. 00, Nno. 00, pp. 1–12, doi: 10.1080/15435075.2022.2154609.

[8] M. Boni, S. Srinivasa Rao, and G. Naga Srinivasulu, 2020, "Performance evaluation of an air breathing–direct methanol fuel cell with different cathode current collectors with liquid electrolyte layer," Asia-Pacific J. Chem. Eng., Vol. 15, No. 4, p. e2465, doi: 10.1002/APJ.2465.

[9] M. Boni, S. S. Rao, and G. N. Srinivasulu, 2021, "Performance evaluation of the incorporation of different wire meshes in between perforated current collectors and membrane electrode assembly on the Passive Direct methanol fuel cell," Chinese J. Chem. Eng., Vol. 32, pp. 360–367, doi: 10.1016/J.CJCHE.2020.07.038.

[10] B. H. Lim, E. H. Majlan, W. R. W. Daud, T. Husaini, and M. I. Rosli, 2016, "Effects of flow field design on water management and reactant distribution in PEMFC: a review," Ionics 2016 223, Vol. 22, No. 3, pp. 301–316, doi: 10.1007/S11581-016-1644-Y.

[11] S. N. Ozdemir and İ. Taymaz, 2021, "CFD Investigation of Different Flow Field Designs for Efficient PEMFC Performance," Sak. Univ. J. Sci., No. June, doi: 10.16984/saufenbilder.901153.

[12] R. Roshandel, F. Arbabi, and G. K. Moghaddam, 2011, "Simulation of an innovative flow-field design based on a bio inspired pattern for PEM fuel cells", doi: 10.1016/j.renene.2011.10.008.

[13] S. R. Badduri, G. N. Srinivasulu, and S. S. Rao, 2020, "Influence of bio-inspired flow channel designs on the performance of a PEM fuel cell," Chinese J. Chem. Eng., Vol. 28, No. 3, pp. 824–831, doi: 10.1016/j.cjche.2019.07.010.

[14] Z. Liao, L. Wei, A. M. Dafalla, J. Guo, and F. Jiang, 2021, "Analysis of the impact of flow field arrangement on the performance of PEMFC with zigzag-shaped channels," Int. J. Heat Mass Transf., Vol. 181, p. 121900, doi: 10.1016/j.ijheatmasstransfer.2021.121900.

[15] W. He, J. S. Yi, and T. Van Nguyen, 2000, "Two-phase flow model of the cathode of PEM fuel cells using interdigitated flow fields," AIChE J., Vol. 46, No. 10, pp. 2053–2064, doi: 10.1002/AIC.690461016.

[16] N. Limjeerajarus and P. Charoen-Amornkitt, 2015, "Effect of different flow field designs and number of channels on performance of a small PEFC," Int. J. Hydrogen Energy, Vol. 40, No. 22, doi: 10.1016/j.ijhydene.2015.04.007.

[17] V. Velisala and G. N. Srinivasulu, 2018, "Numerical Simulation and Experimental Comparison of Single, Double and Triple Serpentine Flow Channel Configuration on Performance of a PEM Fuel Cell," Arab. J. Sci. Eng., Vol. 43, No. 3, doi: 10.1007/s13369-017-2813-7.

[18] M. K. Vijayakrishnan et al., "Numerical and experimental investigation on 25 cm2 and 100 cm2 PEMFC with novel sinuous flow field for effective water removal and enhanced performance," International Journal of Hydrogen Energy, Vol. 45, No. 13. pp. 7848–7862, 2020. doi: 10.1016/j.ijhydene.2019.05.205.

[19] A. Kazim, H. T. Liu, and P. Forges, 1999, "Modelling of performance of PEM fuel cells with conventional and interdigitated flow fields," J. Appl. Electrochem., Vol. 29, No. 12, pp. 1409–1416, doi:

10.1023/A:1003867012551/METRICS.

[20] T. Wilberforce et al., 2019, “A comprehensive study of the effect of bipolar plate (BP) geometry design on the performance of proton exchange membrane (PEM) fuel cells,” Renew. Sustain. Energy Rev., Vol. 111, No. May, pp. 236–260, doi: 10.1016/j.rser.2019.04.081.

[21] M. Liu, H. Huang, X. Li, X. Guo, T. Wang, and H. Lei, 2021, “Geometry optimization and performance analysis of a new tapered slope cathode flow field for PEMFC,” Int. J. Hydrogen Energy, Vol. 46, No. 75, pp. 37379–37392, doi: 10.1016/j.ijhydene.2021.09.022.

[22] A. L. R. Paulino, E. F. Cunha, E. Robalinho, M. Linardi, I. Korkischko, and E. I. Santiago, 2017, “CFD Analysis of PEMFC Flow Channel Cross Sections,” Fuel Cells, Vol. 17, No. 1, pp. 27–36, doi: 10.1002/FUCE.201600141.

[23] J. S. Yi, J. D. Yang, and C. King, 2004, “Water management along the flow channels of PEM fuel cells,” AIChE J., Vol. 50, No. 10, pp. 2594–2603, doi: 10.1002/AIC.10307.

[24] A. Iranzo, C. H. Arredondo, A. M. Kannan, and F. Rosa, “Biomimetic flow fields for proton exchange membrane fuel cells: A review of design trends,” Energy, Vol. 190. Elsevier Ltd, p. 116435, 2020. doi: 10.1016/j.energy.2019.116435.

[25] S. R. Badduri, G. N. Srinivasulu, and S. S. Rao, 2019, “Experimental analysis of PEM fuel cell performance using lung channel design bipolar plate,” Int. J. Green Energy, Vol. 16, No. 15, pp. 1591–1601, doi: 10.1080/15435075.2019.1677238.

[26] M. Marappan et al., 2021, “Performance Studies of Proton Exchange Membrane Fuel Cells with Different Flow Field Designs – Review,” Chem. Rec., Vol. 21, No. 4, pp. 663–714, doi: 10.1002/tcr.202000138.

[27] D. H. Jeon, S. Greenway, S. Shimpalee, and J. W. Van Zee, 2008, “The effect of serpentine flow-field designs on PEM fuel cell performance,” Int. J. Hydrogen Energy, Vol. 33, No. 3, pp. 1052–1066, doi: 10.1016/J.IJHYDENE.2007.11.015.

[28] R. Kumar, A. V. Babu, and S. H. Sonawane, 2022, “Performance evaluation of a trapezoidal interconnector configuration of solid oxide fuel cell: A numerical study,” Int. J. Energy Res., doi: 10.1002/ER.8656.

[29] A. M. Prasad, P. Lavanya, P. Hara Gopal, T. Praveen Sagar, and S. Pavani, 2019, “Experimental investigation of proton exchange membrane (Pem) fuel cell using different serpentine flow channels,” Mater. Sci. Forum, Vol. 969 MSF, pp. 461–465, doi: 10.4028/WWW.SCIENTIFIC.NET/MSF.969.461.

[30] G. Amarnath and A. V. Babu, 2023, “Comparative computational fluid dynamic analysis between split and dual serpentine flow field for proton exchange membrane fuel cells.,” Chem. Pap., [Online]. Available: https://doi.org/10.1007/s11696-023-02841-0

[31] J. M. Sierra, S. J. Figueroa-Ramírez, S. E. Díaz, J. Vargas, and P. J. Sebastian, 2014, “Numerical evaluation of a PEM fuel cell with conventional flow fields adapted to tubular plates,” Int. J. Hydrogen Energy, Vol. 39, No. 29, pp. 16694–16705, doi: 10.1016/j.ijhydene.2014.04.078.

[32] S. Abdulla and V. S. Patnaikuni, 2019, “Detailed analysis of polymer electrolyte membrane fuel cell with enhanced cross-flow split serpentine flow field design,” Int. J. Energy Res., Vol. 43, No. 7, pp. 2806–2820, doi: 10.1002/er.4368.

[33] Ansys, 2009, “Fuel Cells Module Manual,” Manual, No. April.

[34] P. T. Nguyen, T. Berning, and N. Djilali, 2004, “Computational model of a PEM fuel cell with serpentine gas flow channels,” J. Power Sources, Vol. 130, No. 1–2, pp. 149–157, doi: 10.1016/j.jpowsour.2003.12.027.

[35] S. Abdulla, M. Mohan, S. Venkata, and S. Patnaikuni, 2020, “Performance Comparison of PEM Fuel Cell with Enhanced Cross - Flow Split Serpentine and Single Serpentine Flow Field Designs,” Arab. J. Sci. Eng., Vol. 45, No. 9, pp. 7691–7703, doi: 10.1007/s13369-020-04803-0.

[36] L. Wang, A. Husar, T. Zhou, and H. Liu, 2003, “A parametric study of PEM fuel cell performances,” Int. J. Hydrogen Energy, Vol. 28, No. 11, pp. 1263–1272, doi: 10.1016/S0360-3199(02)00284-7.

[37] O. Ryan, C. Suk-Won, C. Whitney, and B. P. Fritz, Fuel cell fundamentals, Third. John Wiley & sons, Inc., Hoboken,New Jersey, 2009. doi: 10.1007/978-0-387-73532-0_1.

[38] F. Barbir, PEM Fuel Cells, Second Edi. 2013. doi: 10.1016/b978-0-12-387710-9.02001-4.

[39] E. E. Kahveci and I. Taymaz, 2018, “Assessment of single-serpentine PEM fuel cell model developed by computational fluid dynamics,” Fuel, Vol. 217, No. August 2017, pp. 51–58, doi: 10.1016/j.fuel.2017.12.073.

[40] X. Liu, H. Guo, F. Ye, and C. F. Ma, 2008, “Flow dynamic characteristics in flow field of proton exchange membrane fuel cells,” Int. J. Hydrogen Energy, Vol. 33, No. 3, pp. 1040–1051, doi: 10.1016/j.ijhydene.2007.11.018.

[41] V. Lakshminarayanan and P. Karthikeyan, 2016, “Optimization of Flow Channel Design and Operating Parameters on Proton Exchange Membrane Fuel Cell Using,” Period. Polytech. Chem. Eng., Vol. 60, No. 3, pp. 173–180, doi: 10.3311/PPch.8461.

[42] Y. Amadane, H. Mounir, A. El Marjani, E. M. Karim, and A. Awan, 2019, “Numerical investigation of hydrogen consumption in Proton Exchange Membrane Fuel Cell by using computational fluid dynamics (CFD) simulation,” Mediterr. J. Chem., Vol. 7, No. 6, pp. 396–415, doi: 10.13171/mjc7618121415ya.

[43] A. Iranzo, M. Muñoz, F. Rosa, and J. Pino, 2010, "Numerical model for the performance prediction of a PEM fuel cell. Model results and experimental validation," Int. J. Hydrogen Energy, Vol. 35, No. 20, pp. 11533–11550, doi: 10.1016/j.ijhydene.2010.04.129.

[44] S. Dutta, S. Shimpalee, and J. W. Van Zee, 2001, "Numerical prediction of mass-exchange between cathode and anode channels in a PEM fuel cell," Int. J. Heat Mass Transf., Vol. 44, No. 11, pp. 2029–2042, doi: 10.1016/S0017-9310(00)00257-X.

[45] S. Shimpalee, S. Greenway, and J. W. Van Zee, 2006, "The impact of channel path length on PEMFC flow-field design," J. Power Sources, Vol. 160, No. 1, pp. 398–406, doi: 10.1016/j.jpowsour.2006.01.099.

[46] Y. Zhu, A. Y. Tremblay, G. A. Facey, and M. Ternan, 2015, "Petroleum Diesel and Biodiesel Fuels Used in a Direct Hydrocarbon Phosphoric Acid Fuel Cell," J. Fuels, Vol. 2015, pp. 1–9, doi: 10.1155/2015/915015.

[47] L. Yuan, Z. Jin, P. Yang, Y. Yang, D. Wang, and X. Chen, 2021, "Numerical analysis of the influence of different flow patterns on power and reactant transmission in tubular-shaped pemfc," Energies, Vol. 14, No. 8, doi: 10.3390/en14082127.